Eur. Phys. J. D **29**, 437–444 (2004)
DOI: 10.1140/epjd/e2004-00040-4

THE EUROPEAN PHYSICAL JOURNAL D

Spatial distribution of quantum fluctuations in spontaneous down-conversion in realistic situations

Comparison between the stochastic approach and the Green's function method

E. Lantz[1,a], N. Treps[2], C. Fabre[2], and E. Brambilla[3]

[1] Laboratoire d'Optique P.M. Duffieux, Institut Femto ST, UMR 6174 du CNRS, Université de Franche-Comté, 25030 Besançon Cedex, France
[2] Laboratoire Kastler Brossel, UMR 8552 du CNRS, Université Pierre et Marie Curie, case 74, 75252 Paris Cedex 05, France
[3] INFM, Dipartimento di Scienze CC.FF.MM., Universitá dell'Insubria, Via Valleggio 11, 22100 Como, Italy

Received 2 October 2003 / Received in final form 15 January 2004
Published online 23 March 2004 –

Abstract. We show that in the limit of negligible pump depletion, the spatial distribution of the quantum fluctuations in spontaneous parametric down-conversion can be computed for any shape of the pump beam by using the Green's function method to linearize the quantum fluctuations, even for very low levels of the intensities measured on the pixels. The results are in complete agreement with stochastic simulations of the Wigner distribution. Both methods show specific quantum effects in realistic situations close to the experiments now in progress, like sub-shot noise correlation between opposite pixels in the far field.

PACS. 42.65.Yj Optical parametric oscillators and amplifiers – 42.50.-p Quantum optics – 42.65.-k Nonlinear optics

1 Introduction

The spatial quantum properties of spontaneous down-conversion (SPDC), or parametric fluorescence, have recently attracted considerable interest. In the photon counting regime, the quantum spatial correlation between the "twin photons" emitted by parametric fluorescence in symmetric directions has been the object of numerous experiments, for example for two-photon imaging [1]. When one uses more powerful pulsed lasers as a pump, the parametric gain is higher and the photons can no longer be separately detected. One uses in this situation low dark noise CCD cameras to record the intensity distribution of the generated field, and the mean number of photons accumulated on each pixel is still very low. If one increases further the pump intensity, one then reaches the domain of "continuous variables", when the measured intensity can be viewed as a continuously varying quantity. In this regime, the fluctuations of the intensities measured on opposite pixels in the far field have been theoretically demonstrated to be correlated well below the quantum level [2] provided that the size of a pixel is greater than the coherence area. Hence, the concept of "twin beams" [3] produced in single transverse mode devices can be generalised to "twin images" [4] in the multimode case. On the experimental side, a strong correlation between spatial fluctuations of the intensity on opposite pixels has been demonstrated on images of SPDC recorded in the far-field on a CCD camera [5,6], though still only at a classical level.

The prediction of the spatial distribution of the quantum fluctuations in realistic situations close to the experimental ones and in the regime of a few photons per pixel is not a simple task, as it involves the calculation of operator mean values that cannot be made analytically in most cases, because of the nonlinear character of parametric interaction. Various approximate theoretical techniques have been used to deal with such problems. Among the most successful ones are the Monte-Carlo simulations of the quantum fluctuations. They rely on the numerical resolution of a stochastic equation for these fluctuations derived in the framework of a given representation, such as the P, positive-P or Wigner representation [7]. Another powerful technique is the so-called semi-classical or linearization method. It is based on the fact that the quantum moments of the Wigner distribution, corresponding to symmetrically-ordered operators, can be calculated by propagation of classical fields in the limit of weak quantum fluctuations with respect to the input fields. This linearization method, which is widely used to treat single mode problems [8], is at first sight limited to the case of intense fields. It has been recently employed to calculate the spatial distribution of the quantum fluctuations in a spatial soliton [9] and in the Optical Parametric Oscillator below threshold [10]. In this latter case however, the mean value

[a] e-mail: elantz@univ-fcomte.fr

of the signal field is zero and the linearization procedure corresponds to neglecting pump depletion, showing that linear and linearized systems can be described in similar ways.

The purpose of this paper is to extend the Green's function method used in the spatial soliton case to the problem of spontaneous down-conversion in a travelling wave amplifier with a non ideal profile of the pump beam, and to compare its results with stochastic simulations proposed in references [11,12], in order to be able to make reliable predictions of the results of experiments currently in progress in Besançon [13] and Como [14]. In Section 2, we will recall the main aspects of the linear approach and show how to extend it to the problem of SPDC using a Green's function approach. In Section 3 we make a brief review of the stochastic method, and compare in Section 4 the results of the two methods. While the Green's function method gives directly the quantum moments of fluctuations, the stochastic images exhibit spatial statistical fluctuations, like the experimental images. Section 5 compares the statistical properties of these spatial fluctuations with the quantum moments calculated with the Green's function method. In Section 6, we conclude by stressing some advantages and drawbacks of the two methods and give some directions for the development of these methods.

2 Linear approach of parametric fluorescence

The classical propagation equation of the positive frequency field envelope A of the sub-harmonic field in the paraxial approximation is given by [15]:

$$i\frac{d}{dz}A(\vec{r},z)+\frac{1}{2k}\nabla_T^2 A(\vec{r},z)=\frac{\omega^2}{kc^2}d_{eff}A_p(\vec{r},z)A^*(\vec{r},z)e^{-i\Delta kz} \quad (1)$$

where A_p is the pump field at frequency 2ω, d_{eff} is the effective nonlinear coefficient in the considered direction, Δk is the collinear phase-mismatch vector, z the main propagation direction, $\vec{r}$ the transverse position and ∇_T^2 the transverse Laplacian. In the undepleted pump approximation, the pump field A_p is not affected by the interaction and can be treated as a classical variable. This situation is similar to the problem of the OPO below threshold [10]. Assuming that in equation (1) A_p is independent of z, one then obtains the following quantum linear equation by replacing the field A by its quantum operator counterpart:

$$i\frac{d}{dz}\hat{A}(\vec{r},z)+\frac{1}{2k}\nabla_T^2 \hat{A}(\vec{r},z)=\frac{\omega^2}{kc^2}d_{eff}A_p(\vec{r})\hat{A}^\dagger(\vec{r},z)e^{-i\Delta kz}. \quad (2)$$

This equation is also valid when one replaces $\hat{A}(\vec{r},z)$ and $\hat{A}^\dagger(\vec{r},z)$ respectively by the annihilation and creation operators $\hat{a}(\vec{r},z)$ and $\hat{a}^\dagger(\vec{r},z)$ of a photon at point $(\vec{r},z)$, because these operators are proportional. These creation and annihilation operators verify [16]:

$$\left[\hat{a}(\vec{r},z),\hat{a}^\dagger(\vec{r}\,',z)\right]=\delta(\vec{r}-\vec{r}\,'),\quad [\hat{a}(\vec{r},z),\hat{a}(\vec{r}\,',z)]=0. \quad (3)$$

We consider in this paper single temporal modes, so that the calculated mean values have only a spatial variation. This simplified situation corresponds to measurements performed by a CCD camera on light integrated over the duration of the pump pulse and filtered in wavelength in order to obtain a minimum time-bandwidth product. We have shown [13] that the experimental distribution of spatial fluctuations in such a case corresponds to the single-mode statistics of SPDC.

Let us now consider a non linear crystal of length l, and let us call $\hat{a}_{in}(\vec{r})$ and $\hat{a}_{out}(\vec{r})$ the annihilation operators at the input ($z=0$) and output ($z=l$) of the crystal, respectively. In the undepleted pump approximation and in the absence of losses [17], the output operators can be expressed as linear functions of the input operators:

$$\begin{aligned}\hat{a}_{out}(\vec{r})&=\int d\vec{r}_1\ \left[G(\vec{r},\vec{r}_1)\hat{a}_{in}(\vec{r}_1)+H(\vec{r},\vec{r}_1)\hat{a}_{in}^\dagger(\vec{r}_1)\right]\\ \hat{a}_{out}^\dagger(\vec{r})&=\int d\vec{r}_1\ \left[G^*(\vec{r},\vec{r}_1)\hat{a}_{in}^\dagger(\vec{r}_1)+H^*(\vec{r},\vec{r}_1)\hat{a}_{in}(\vec{r}_1)\right]\end{aligned} \quad (4)$$

where G and H are the Green's functions of the propagation equation (2).

The quantum spatial correlations in the intensity fluctuations are then described by the normally ordered covariance function $\tilde{C}(\vec{r},\vec{r}\,')$ between two points of the far field. By making use of a general property characterizing fields with a Gaussian statistics [18], it can be expressed as a sum of products of second-order covariance functions:

$$\begin{aligned}\tilde{C}(\vec{r},\vec{r}\,')&=\langle :\delta\hat{N}(\vec{r})\delta\hat{N}(\vec{r}\,'):\rangle\\ &=|\langle\hat{a}_{out}^\dagger(\vec{r})\hat{a}_{out}(\vec{r}\,')\rangle|^2+|\langle\hat{a}_{out}(\vec{r})\hat{a}_{out}(\vec{r}\,')\rangle|^2\end{aligned} \quad (5)$$

where $\hat{N}$ is the photon number operator. The symbol $:\ :$ denotes normal ordering (n.o.). In particular, the n.o. variance $\tilde{C}(\vec{r},\vec{r})$ implies the subtraction of the shot noise to the total variance. The mean value is taken over the quantum state present at the input of the crystal, which is here the vacuum at all points of the input transverse plane. The second-order covariance functions appearing in equation (5) can then be easily calculated in terms of the Green's functions:

$$\begin{aligned}\langle\hat{a}_{out}^\dagger(\vec{r})\hat{a}_{out}(\vec{r}\,')\rangle&=\int d\vec{r}_1\ [H^*(\vec{r},\vec{r}_1)H(\vec{r}\,',\vec{r}_1)]\\ \langle\hat{a}_{out}(\vec{r})\hat{a}_{out}(\vec{r}\,')\rangle&=\int d\vec{r}_1\ [G(\vec{r},\vec{r}_1)H(\vec{r}\,',\vec{r}_1)]\end{aligned} \quad (6)$$

where the free-field commutation relation (3) has been used.

Let us now introduce the two quadrature operators, q_{out} and p_{out}, which are given by:

$$\hat{q}_{out}(\vec{r}) = \frac{\hat{a}_{out}(\vec{r}) + \hat{a}^{\dagger}_{out}(\vec{r})}{\sqrt{2}}$$
$$\hat{p}_{out}(\vec{r}) = \frac{i(\hat{a}^{\dagger}_{out}(\vec{r}) - \hat{a}_{out}(\vec{r}))}{\sqrt{2}}. \quad (7)$$

These Hermitian operators can be expressed in terms of the Green's functions as follows:

$$\begin{aligned}\hat{q}_{out}(\vec{r}) &= \frac{1}{\sqrt{2}} \int d\vec{r}_1 \Big[\{G(\vec{r},\vec{r}_1) + H^*(\vec{r},\vec{r}_1)\}\, \hat{a}_{in}(\vec{r}_1) \\ &\quad + \{G(\vec{r},\vec{r}_1) + H^*(\vec{r},\vec{r}_1)\}^*\, \hat{a}^{\dagger}_{in}(\vec{r}_1)\Big] \\ &= \int d\vec{r}_1 \Big[\mathrm{Re}\,\{G^*(\vec{r},\vec{r}_1) + H(\vec{r},\vec{r}_1)\}\, \hat{q}_{in}(\vec{r}_1) \\ &\quad + \mathrm{Im}\,\{G^*(\vec{r},\vec{r}_1) + H(\vec{r},\vec{r}_1)\}\, \hat{p}_{in}(\vec{r}_1)\Big] \quad (8)\end{aligned}$$

and

$$\begin{aligned}\hat{p}_{out}(\vec{r}) &= \frac{i}{\sqrt{2}} \int d\vec{r}_1 \Big[\{H^*(\vec{r},\vec{r}_1) - G(\vec{r},\vec{r}_1)\}\, \hat{a}_{in}(\vec{r}_1) \\ &\quad + \{G^*(\vec{r},\vec{r}_1) - H(\vec{r},\vec{r}_1)\}\, \hat{a}^{\dagger}_{in}(\vec{r}_1)\Big] \\ &= \int d\vec{r}_1 \Big[\mathrm{Im}\,\{G(\vec{r},\vec{r}_1) - H^*(\vec{r},\vec{r}_1)\}\, \hat{q}_{in}(\vec{r}_1) \\ &\quad + \mathrm{Re}\,\{G(\vec{r},\vec{r}_1) - H^*(\vec{r},\vec{r}_1)\}\, \hat{p}_{in}(\vec{r}_1)\Big] \quad (9)\end{aligned}$$

where Re and Im denote the real and the imaginary part.

The propagation of these quadrature operators is governed by equation (2). However, the similar form of equations (1, 2) implies that their corresponding Green's functions are the same. Hence, one can directly numerically compute the value of the Green's functions using a delta function successively on both quadratures as an initial condition [9] in the classical propagation equation (1). In this classical equation, the phase of the input quadratures q_{in} and p_{in} corresponds respectively to a maximum amplification or deamplification. The output quadrature fields obtained through the numerical propagation of this delta-like input functions are directly proportional to linear combinations of the Green's functions. It is then easy to deduce the actual value of G and H after the numerical propagation of a delta function centered at each point of the transverse plane.

To summarize this section, the Green's functions H and G can be numerically computed as linear combinations of output fields obtained by propagation of delta function input fields. The propagation of these input fields must be computed for each position in the output crystal plane and for both input quadratures. The knowledge of these Green's functions allows us to compute all the output covariance functions.

3 Stochastic simulation of the fluctuations

In the linear approximation, one can show [7] that the Wigner distribution of the output field can be simulated simply by integrating the classical propagation equations starting from a stochastic field which has the phase-space distribution determined by the input field Wigner function. In the following we shall denote with α the stochastic field and with $\langle\ldots\rangle_{stoch}$ the corresponding stochastic averages, in order to distinguish them from quantum-mechanical operators and their expectation values, denoted as usual with $\langle\ldots\rangle$ and $\hat{a}$. Within the Wigner representation we have the identification between the different moments of the stochastic field and the expectation values of the corresponding symmetrized operator:

$$\langle\ldots\rangle_{stoch} \leftrightarrow \langle\ldots\rangle_{SYMMETRIZED\ \ OPERATORS}\,. \quad (10)$$

In the discretized model used in the numerical simulations the position coordinates $\vec{r}$ becomes a discrete index indicating the pixel of the numerical grid (or the square pixels of a CCD camera) and the continuous fields $a(\vec{r})$ and $\alpha(\vec{r})$ are replaced with the discrete field $a_{\vec{r}}$ and $\alpha_{\vec{r}}$ respectively, which we define according to the relation

$$\hat{a}_{\vec{r}} = \frac{1}{\sqrt{\Delta S}} \int_{R(\vec{r})} \hat{a}(\vec{r},z), \quad \alpha_{\vec{r}} = \frac{1}{\sqrt{\Delta S}} \int_{R(\vec{r})} \alpha(\vec{r},z). \quad (11)$$

The integrals on the r.h.s. are performed on the considered pixel region $R(\vec{r})$ and ΔS denotes the pixel area. With such a normalization and assuming that ΔS is small compared to the field scale of variation, $\hat{a}^{+}_{\vec{r}}\hat{a}_{\vec{r}}$ gives the mean number of photons detected in pixel $\vec{r}$ and commutation relations (3) become

$$\left[\hat{a}_{\vec{r}}, \hat{a}^{+}_{\vec{r}'}\right] = \delta_{\vec{r},\vec{r}'}, \quad [\hat{a}_{\vec{r}}, \hat{a}_{\vec{r}'}] = 0, \quad (12)$$

where $\delta_{\vec{r},\vec{r}'}$ denotes the Kronecker's symbol. In general the quantities measured in an experiment do not correspond to symmetrized operators, so that correction terms must be added to the averages made on the stochastic fields to obtain the desired ordering. For example, according to relation (11) and commutation rules (12), the expectation of the photon number in pixel $\vec{r}$ is given by

$$\left\langle \hat{a}^{+}_{\vec{r}}\hat{a}_{\vec{r}} \right\rangle = \left\langle \alpha^*_{\vec{r}}\,\alpha_{\vec{r}} \right\rangle_{stoch} - \frac{1}{2}. \quad (13)$$

Similarly, the discretized version of the n.o. photon number covariance functions defined in equation (5) is obtained from the relation

$$\begin{aligned}\tilde{C}_{\vec{r},\vec{r}'} &\equiv \left\langle \hat{a}^{+}_{\vec{r}}\hat{a}^{+}_{\vec{r}'}\hat{a}_{\vec{r}'}\hat{a}_{\vec{r}} \right\rangle - \left\langle \hat{a}^{+}_{\vec{r}}\hat{a}_{\vec{r}} \right\rangle \left\langle \hat{a}^{+}_{\vec{r}'}\hat{a}_{\vec{r}'} \right\rangle \\ &= \left\langle \alpha^*_{\vec{r}}\,\alpha_{\vec{r}}\,\alpha^*_{\vec{r}'}\,\alpha_{\vec{r}'} \right\rangle_{stoch} - \left\langle \alpha^*_{\vec{r}}\,\alpha_{\vec{r}} \right\rangle_{stoch} \left\langle \alpha^*_{\vec{r}'}\,\alpha_{\vec{r}'} \right\rangle_{stoch} \\ &\quad - \delta_{\vec{r},\vec{r}'} \left[\left\langle \alpha^*_{\vec{r}}\,\alpha_{\vec{r}} \right\rangle_{stoch} - \frac{1}{4} \right]. \quad (14)\end{aligned}$$

To perform the Monte-Carlo numerical simulations, we proceed with the following steps:

– we generate the stochastic input field with the appropriate phase-probability distribution corresponding to the vacuum field in the Wigner representation, i.e. Gaussian white noise with zero mean and a random phase, such that $\langle \alpha^*_{\vec{r}}\,\alpha_{\vec{r}} \rangle_{stoch} = 1/2$, in agreement with equation (13);

– the propagation of the stochastic field is then evaluated by integrating the classical propagation equation (1), which are solved with a split-step algorithm;
– the expectations of the symmetrically ordered operators are estimated by averaging the results over a great number of trajectories (10 [4] in the present paper). The procedure must indeed be reiterated a sufficiently large number of times, so that the stochastic averages performed on the output field become good approximations to the corresponding quantum expectation values;
– following the examples of equations (13, 14), all the expectation values of the covariance functions in the desired ordering are then obtained from these stochastic averages by applying the appropriate corrections which can be derived using relation (10) and commutation rules (12).

We note finally that the single trajectories of the Monte-Carlo simulation reproduce well the spatial features of SPDC obtained experimentally from a single pump shot in the high gain regime.

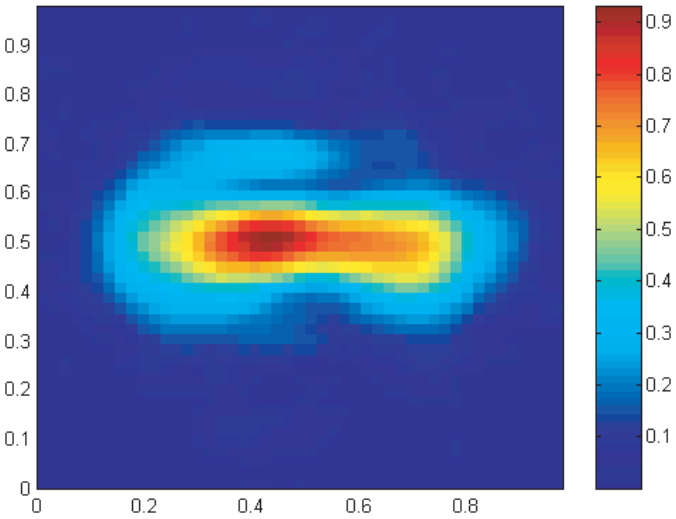

Fig. 1. Experimental cartography of the pump field. The intensity is given in arbitrary units and the lateral dimensions are given in mm.

4 Comparison between the two approaches

While the formalism presented in Section 2 can be applied to calculate near-field expectations (i.e. intensities in the image of the output face of the crystal) as well as far-field expectations (Fourier plane), all presented results will be given in the far-field, because quantum effects are more visible in this plane [1]. The formalism of Section 2 can be applied without difficulties to this configuration, simply by making a Fourier transform of the fields at the output.

Figure 1 presents the near field image of the pump beam intensity that we have employed in all the simulations. Its phase is assumed to be constant over all the transverse plane. This pump beam, recorded in our previous experimental works [6], is strongly elliptical, with an horizontal dimension much greater than the vertical one. In the present paper, its intensity has been chosen in order to ensure a low parametric fluorescence, where quantum effects are stronger. More precisely, the maximum gain in amplitude on the amplified quadrature is $\exp(g_{max}l) = 5.5$, giving a maximum number of output photons per spatial mode of $\mathrm{sh}^2(gl) = 7$.

The crystal, which has a length $l = 2$ mm, is supposed to be oriented in such a way that one has perfect phase matching in directions making a cone with respect to the main propagation direction. The pixellisation of the image plane must be performed at a spatial frequency sufficiently greater than twice that corresponding to phase-matching bandwidth [19]. Because the proposed computation method uses four dimensional arrays (2 points with 2 transverse coordinates), the number of pixels has been limited to 48×48.

Figure 2a presents the computed mean intensity of parametric fluorescence in the far field, given by the first of equations (6) with $\vec{r} = \vec{r}'$. As expected, the shape reproduces the gain variation due to the phase-matching conditions: the ring shape corresponds a crystal oriented in order to obtain non collinear phase-matching. From this mean intensity we can deduce the size of a coherence area as follows. The maximum gain in amplitude, for perfect phase-matching, on the amplified quadrature is $\exp(g_{max}l) = 5.5$, giving a maximum number of output photons per spatial mode of $\mathrm{sh}^2(g_{max}l) = 7$. In the far field, these photons spread out in a coherence area, whose size scales as the inverse of the size of the fluorescence beam in the near field. Hence, the sum of the mean intensity, expressed in photons per pixel, on all pixels in a coherence area corresponds to the number of photons in one mode and the coherence area can be estimated as the ratio between the number of photons for perfect phase matching in one mode and the maximum mean intensity per pixel. The result is $7/0.32 = 22$ pixels per coherence area. This size is much smaller than in the experiments of reference [5], with the same pump shape, because the crystal length and the mean pump intensity are smaller in the present simulation than in these experiments, resulting in a larger, though less intense, fluorescence beam at the output face of the crystal and in a narrower coherence area in the far field.

Figure 2b presents the results obtained by the stochastic method, following the procedure indicated above, in the same conditions as in Figure 2a. We can observe that there is a very good agreement between the two results, in intensity and size, even when the mean is very close to zero, within statistical errors corresponding to the number of shots used in the average.

Figures 3a and 3b present the same type of comparison, but now for the n.o. variance, i.e. the difference between the variance and the shot noise $\tilde{C}_{\vec{r},\vec{r}} = \langle : (\delta\hat{N}_{\vec{r}})^2 : \rangle$. Figures 3a and 3b are respectively obtained using the Green's function and the stochastic methods, and one observes again a good agreement between them, both in size and intensity. A striking point is that the value of the

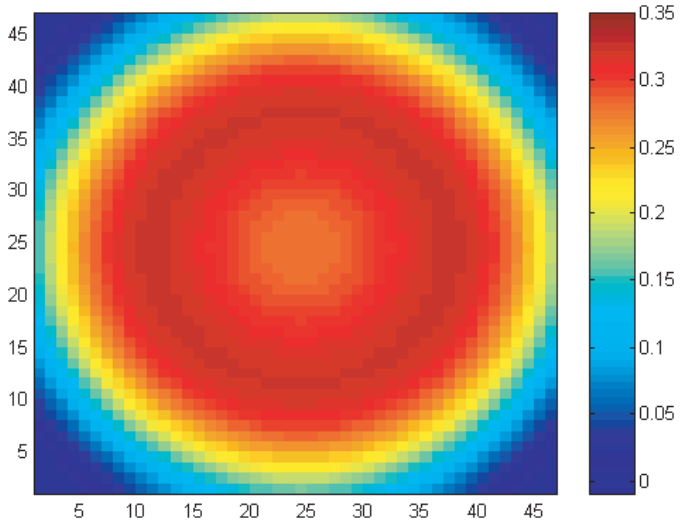

(a)

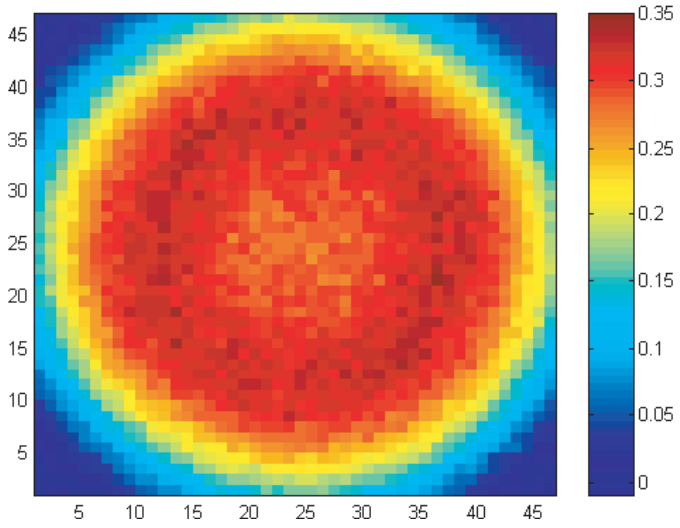

(b)

Fig. 2. (a) Mean intensity in the far field, in photons per pixel, determined by the Green's function method. The coordinates are graduated in pixels. The pixel size p is given in angle units by the laws of Fourier optics: $p = \lambda/L$, where $\lambda = 1.064$ μm is the wavelength and $L = 1$ mm the lateral size of the sampled crystal area in the near-field. (b) Mean intensity in the far field determined by the stochastic method, averaged over 10 000 shots, with the same units as (a).

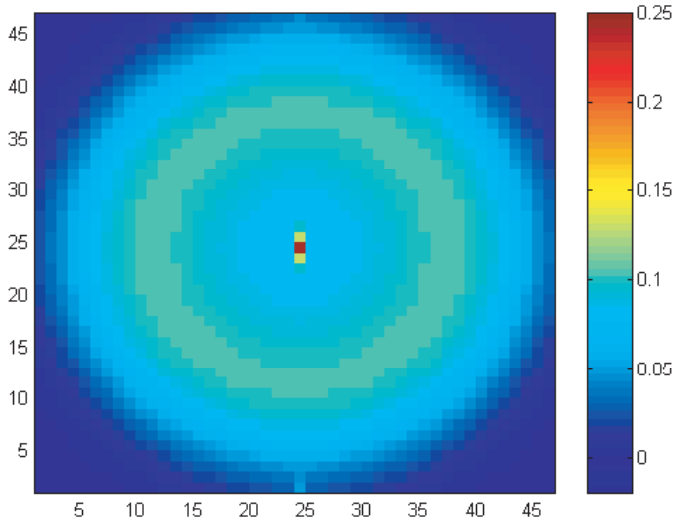

(a)

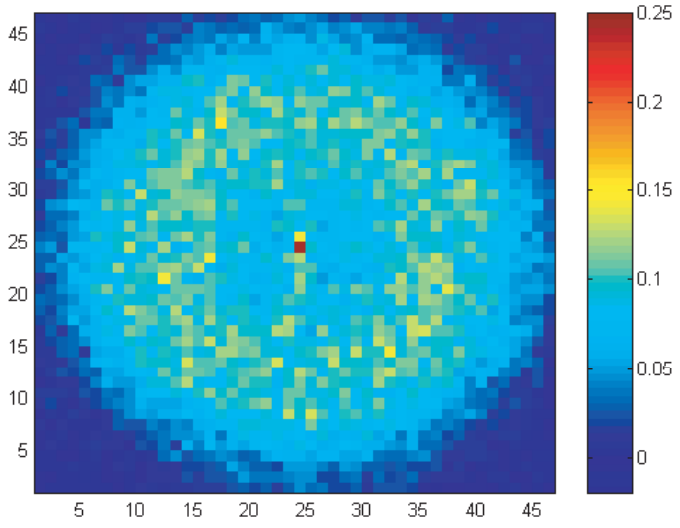

(b)

Fig. 3. Distribution of $\tilde{C}(\vec{r}, \vec{r}\,' = \vec{r}) = \langle :(\delta\hat{N}(\vec{r}))^2: \rangle$ in the far field plane (same conditions as in Fig. 2). (a) Green's function method; (b) stochastic average.

variance is roughly doubled on the pixel at the centre. This feature is confirmed by an analytical calculation, detailed in Appendix: the second term in equation (5) gives a contribution at the origin where opposite pixels merge, while it vanishes elsewhere.

Figure 4 provides the same comparison, but now for the intensity correlations between different pixels, represented by the measure of the covariance function $\tilde{C}(\vec{r}, \vec{r}\,')$ (Eq. (5)) for any value of $\vec{r}\,'$ and a particular value of $\vec{r}$ ($\vec{r} = (x, y) = (22, 18)$). Here also, there is a very good agreement between the two results. One observes, as expected, that there exist strong correlations between the considered pixel and the symmetrical one with respect to the propagation axis. One also observes, as already quoted in reference [1], that the covariance between opposite points (signal-idler covariance, $\tilde{C}_{\vec{r},-\vec{r}}$) is larger than the covariance between nearby points (signal-signal n.o. variance, $\tilde{C}_{\vec{r},\vec{r}}$) [20]. This property has no classical counterpart [2]. One can also clearly see that the elliptical shape of the pump beam results in stretching the shape of the covariance area in the orthogonal direction, as expected in the Fourier plane.

The existence of this large covariance peak implies that the variance V_- on the difference between the intensities recorded on opposite pixels is significantly below the shot noise level, provided that the pixel has a sufficient size to include at least a coherence area [2]. If it is not the case, pixels must be binned to increase the detection area.

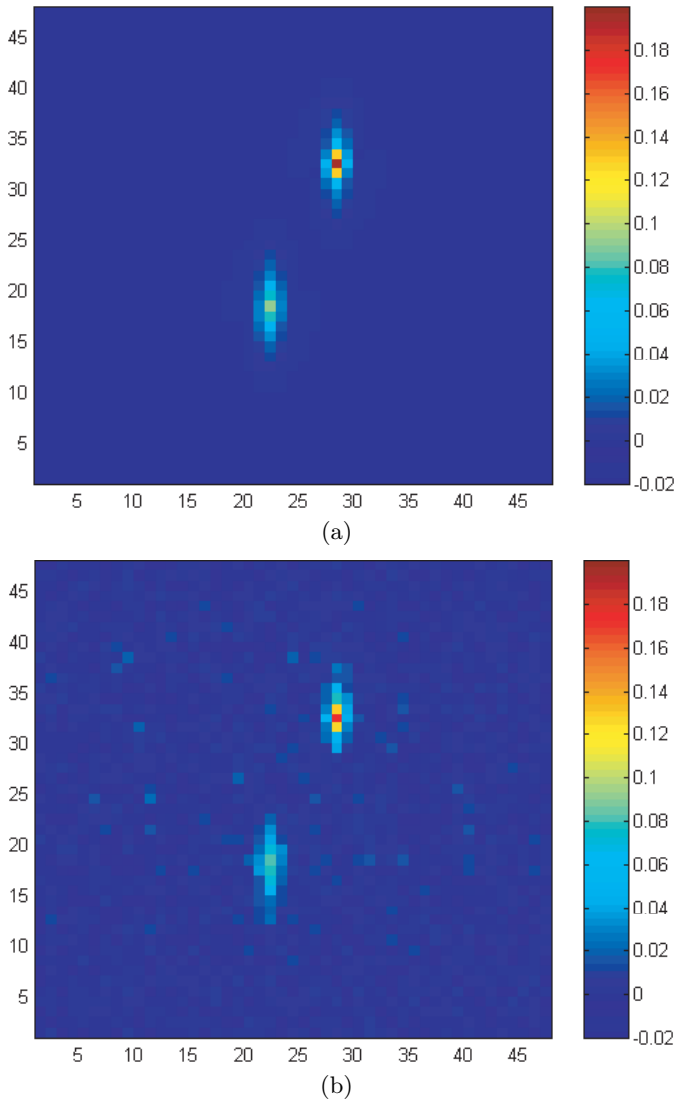

Fig. 4. Covariance between intensity fluctuations measured on pixel ($x = 22$, $y = 18$) and all the other pixels, (in square photons) (same conditions as in Fig. 2). (a) Green's function method; (b) stochastic average.

In order to correspond to an experimentally measurable quantity, V_- is defined as including the shot noise terms, and not only the n.o. covariance terms. After binning, V_- reads as:

$$V_- = SN_- + \sum_{\vec{r}} \sum_{\vec{r}'} \left[\tilde{C}_{\vec{r},\vec{r}'} + \tilde{C}_{-\vec{r},-\vec{r}'} - 2\tilde{C}_{\vec{r},-\vec{r}'} \right] \quad (15)$$

with

$$SN_- = \sum_{\vec{r}} N_{\vec{r}} + \sum_{\vec{r}} N_{-\vec{r}}. \quad (16)$$

The sum over $\vec{r}$ and $\vec{r}'$ is extended to the binned pixels composing one of the two symmetrical detection area, and $\tilde{C}_{\vec{r},\vec{r}}$ is the covariance between two pixels defined in equation (14). Equation (16) expresses in a standard way the covariance of a difference. SN_- represents the shot noise contribution on the two detection areas, while the last three terms in equation (16) determine the contributions due to the field correlations. The sum over these last three terms is negative, leading to the sub-shot noise value of V_-.

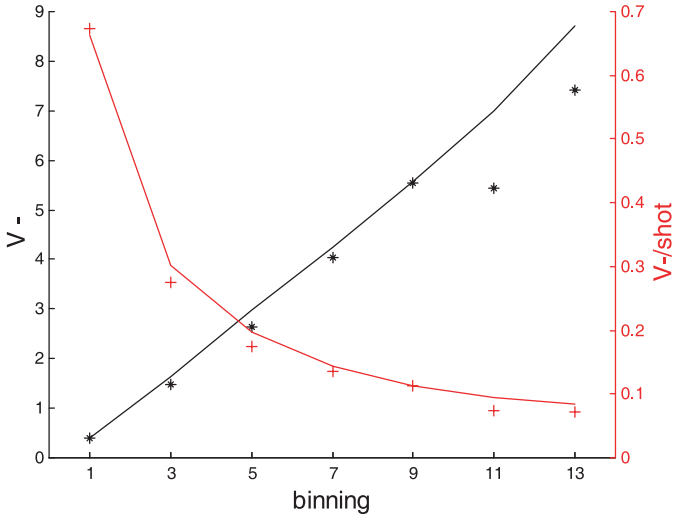

Fig. 5. Plot of the variance V_- evaluated for two symmetrical square detection area of $n \times n$ binned pixels as a function of n. The first area is centred in ($x = 22$, $y = 18$). Full lines: Green's function method. Stars and cross: stochastic averages. The data in red give the ratio between this variance V_- and the shot noise level SN_-.

For the stochastic averages, the formulae are simpler, because the total number of photons on a pixel after binning can be easily computed for each shot, as well as the difference between the energy of two opposite pixels. Hence V_- is simply given by the variance of this difference. However the corrections for symmetrically ordering the operators must take into account the binning and the difference: the corrections on the mean and on the variance scale as the number of binned pixels (the total number on both the signal and the idler for V_-).

Figure 5 gives the results for the pixel centred at ($x = 22$, $y = 18$) and its opposite. We have verified that the small differences between both methods are uniquely due to the residual random character of the averages (for example in the case of a 9×9 binning, using the 5000 first shots gives a V_- of 4.53, instead of 5.55 for 10 000 shots). As expected, the ratio V_-/SN_- decreases when the number of binned pixels is increased. For a pixel much smaller than the coherence area, it has been shown [2] that the contribution due to the correlation terms on the r.h.s. of equation (16) becomes negligible compared to SN_- and V_- tends to the shot noise level. In the opposite situation, when the binned pixels cover an area which is large compared to the coherence area, the effect of correlations becomes relevant and the ratio between V_- and the level of shot noise goes to zero. Here, a 5×5 binning corresponds roughly to a coherence area, which has an estimated surface of 22 pixels.

Table 1. Labels (1): values of the variance from the Green's function method (with shot-noise or after subtracting the mean, which gives the departure from the shot noise) of a pixel on a circle in one image and of the covariance of one pixel with its opposite in one image. Labels (2): expectation values from the stochastic approach of the corresponding variance without and with normal ordering [n.o.], and of the covariance between opposite points on the circle, averaged over 10 000 shots.

Circle diameter (pixels)	$V(1)$	$V(2)$	$V(1)$ [n.o.]	$V(2)$-mean	Cov (1)	Cov (2)
15	0.394	0.382	0.092	0.080	0.194	0.174
30	0.417	0.411	0.100	0.093	0.211	0.200
39	0.323	0.329	0.066	0.067	0.150	0.150

5 Assessment of spatial fluctuations

All the above-presented results deal with the variation of the energy on one pixel from one shot to another. However, the information on a weak image is corrupted by the spatial fluctuations even in one shot and it is important to assess the statistical properties of these spatial fluctuations. Only the stochastic method provides this assessment, because the Green's function method gives directly the expectation values of the pixels, that are not random quantities in one image. We will see however that some kind of ergodicity holds in the present case, and that the fluctuations measured on pixels from one shot to another or within an image have the same statistical behaviour. To ensure that all pixels used in the statistics have the same expectation value, we use only pixels on a circle centred on the optical axis. For each shot, the variance is calculated for the pixels on the circle. Then the values for 10 000 shots are averaged and the appropriate corrections are performed. The procedure is repeated for the covariance between opposite pixels and the results are compared to that of the Green's function method for one pixel (variance as in Fig. 3 and covariance between opposite pixels as in Fig. 4).

Table 1 gives the corresponding results for three circles, corresponding to three different phase-matching conditions. One observes that the values from the stochastic approach are close to that obtained by the Green's function method for one pixel of the corresponding circle. However, there is a large dispersion of the obtained variances: in other words, they strongly vary from one shot to another (including negative values for the corrected variance). For example the standard deviation of the variance on the circle with a diameter of 15 pixels is 0.19, i.e. more than twice the mean variance. This standard deviation is due to the small number of independent spatial modes that are involved in the estimation of each one-shot spatial variance. However, the almost equality between the average of the one-shot variances and the shot to shot variance confirms that the statistical behaviour is the same in both cases.

6 Conclusion

The spatial quantum properties of parametric fluorescence are now well investigated, at least at the theoretical level. However, obtaining numerical values likely to be compared with actual experimental situations implies the need to be able to simulate realistic non ideal situations with, for example, a non circular shape of the pump beam. We have shown that at the limit where the pump depletion is negligible two approaches can be used to predict the results in such situations. The Monte-Carlo simulation of the Wigner representation gives the quantum moments at the limit of a great number of random realisations after averaging and appropriate corrections to take into account operator ordering. In the limit of an infinite number of random realisations, its results converge to those of the Green's function method. Moreover, the Monte-Carlo method reproduces to some extent the spatial fluctuations of the image on one shot, at least for high gains. For lower gains where ordering corrections are not negligible, the connection between a simulated image from one shot and its experimental counterpart is much less straightforward and a correct simulation of such an experimental image appears as an unsolved and difficult problem.

The Green's function method presented in this paper has the advantage of directly giving the expectation values, without any averaging of random images, even when the mean number of photons detected on the pixels is very low. The extension of the Green's function method to the time-domain is easy in principle; however, it would imply 6-dimensional arrays, that could lead to numerical problems with many temporal modes. Hence, both methods appear complementary to apply to quantum optics the numerical methods that allow the simulation of propagation of classical fields in realistic non ideal situations.

This work has been supported by the European Union in the frame of the Quantim network (contract IST 2000-26019).

Appendix

We show in this annex that equation (5) implies a n.o. variance at the center of the far field that takes a value about twice that of its neighbours.

We start from the analytic expression of the far field obtained in the focal plane of a lens set at a distance f from the crystal outpout face, f being the focal length of the crystal:

$$\hat{a}_{out}(\vec{r}) = \frac{2\pi i}{\lambda f} \int d\vec{r}\,' p(\vec{r}-\vec{r}\,') \times \left(u(\vec{r}\,') a_{in}\left(\frac{2\pi\vec{r}\,'}{\lambda f}\right) + v(\vec{r}\,') a_{in}^{\dagger}\left(-\frac{2\pi\vec{r}\,'}{\lambda f}\right)\right). \quad \text{(A.1)}$$

This input-output relation has been derived in reference [2] within the framework of the plane-wave pump approximation. λ is the signal wavelength and the response function $p(\vec{r})$ is the far field diffraction pattern due to a fictitious pupil of area S_{pupil} set on the crystal output face. This pupil is used to take into account the finite size of the system in the transverse plane and can be identified with the effective cross-section area of the pump beam. $u(\vec{r})$ and $v(\vec{r})$ are gain functions determined by the phase matching conditions inside the crystal and obey the usual unitary relation $|u(\vec{r})|^2 - |v(\vec{r})|^2 = 1$. As in reference [2], we assume that the effect of diffraction is sufficiently small to consider these gain functions as constants in the integration of equation (A.1). The following approximations can then be used:

$$|p(\vec{r})| = \delta(\vec{r}), \quad |p(\vec{r})|^2 = \frac{1}{S_{diff}}\delta(\vec{r}) \tag{A.2}$$

where $S_{diff} = (\lambda f)^2/S_{pupil}$ denotes the area of the diffraction pattern. Applying the same commutation rules as equation (3) for $a_{in}(\vec{q})$ and using equations (A.1, A.2), we find that the second term in the r.h.s of equation (5) vanishes everywhere except in the origin, when this equation describes the n.o. variance. More precisely we obtain

$$|\langle \hat{a}_{out}(\vec{r})\hat{a}_{out}(\vec{r})\rangle|^2 = \begin{cases} 0, & \vec{r} \neq 0, \\ \left(\frac{1}{S_{diff}}|u(\vec{r})v(\vec{r})|\right)^2, & \vec{r} = 0. \end{cases} \tag{A.3}$$

For $\vec{r} = 0$, this term adds to the first term in equation (5), this first term being proportional to v^4. In the numerical results of this paper, $v^2_{max}(\vec{r}) = \mathrm{sh}^2(g_{max}l) = 7$, giving $v^2(\vec{r} = 0) \approx 6$ (see Fig. 2a) and $(u(0)v(0))^2 \approx 42$. Hence, the n.o. variance is more than doubled at the center of the far-field, as it is clearly visible in Figure 3. This doubling occurs on an area of the order of S_{diff} and can be explained by noting that the collinear mode $\vec{q} = 0$ is fully degenerate.

References

1. A.F. Abouraddy, B.E.A. Saleh, A.V. Sergienko, M.C. Teich, J. Opt. Soc. Am. B **19**, 1174 (2002)
2. E. Brambilla, A. Gatti, L.A. Lugiato, Eur. Phys. J. D **15**, 127 (2001)
3. A. Heidmann, R.J. Horowicz, S. Reynaud, E. Giacobino, C. Fabre, G. Camy, Phys. Rev. Lett. **59**, 2555 (1987); O. Aytür, P. Kumar, Phys. Rev. Lett. **65**, 1551 (1990)
4. A. Gatti, E. Brambilla, L.A. Lugiato, M.I. Kolobov, Phys. Rev. Lett. **83**, 1763 (1999)
5. B.M. Jost, A.V. Sergienko, A.F. Abouraddy, B.E.A. Saleh, M.C. Teich, Opt. Expr. **3**, 81 (1998)
6. F. Devaux, E. Lantz, Eur. Phys. J. D **8**, 117 (2000)
7. D.F. Walls, G.J. Milburn, *Quantum Optics* (Springer Verlag, Berlin, 1994)
8. S. Reynaud, A. Heidman, E. Giacobino, C. Fabre, Progr. Opt. **30**, 3 (1992)
9. N. Treps, C. Fabre, Phys. Rev. A **62**, 033816 (2000)
10. A. Gatti, H. Wiedemann, L.A. Lugiato, I. Marzoli, G.L. Oppo, S.M. Barnett, Phys. Rev. A **56**, 877 (1997)
11. E. Lantz, F. Devaux, Eur. Phys. J. D **17**, 93 (2001)
12. E. Brambilla, A. Gatti, M. Bache, L.A. Lugiato, Phys. Rev. A **69**, 023802 (2004)
13. A. Mosset, F. Devaux, G. Fanjoux, E. Lantz, Eur. Phys. J. D **28**, 447 (2004)
14. O. Jedrikiewicz, Y. Jiang, P. Di Trapani, E. Brambilla, A. Gatti, L.A. Lugiato, EH5-4-THU, CLEO/EQEC 2003, Munich
15. A. Yariv, *Quantum Electronics*, 3rd edn. (John Wiley & Sons, 1988), Chaps. 16 and 17
16. M.I. Kolobov, Rev. Mod. Phys. **71**, 1539 (1999)
17. If losses were present (for example absorption), coupling with a vacuum operator would have to be introduced in order to preserve the unitary conditions. See: M.I. Kolobov, L.A. Lugiato, Phys. Rev. A **52**, 4930 (1995). In this reference, this operator resulted from a finite pupil after the crystal and had no consequence on any normally-ordered correlation function. However, losses inside the crystal would imply a different situation, with actual parametric fluorescence generated from this introduced vacuum. This situation is outside the scope of the paper
18. C. Gardiner, *Quantum noise* (Springer, Berlin, 1991)
19. F. Devaux, E. Lantz, Opt. Commun. **114**, 295 (1995)
20. Note that this property vanishes for higher gains: $\tilde{C}_{\vec{r},\vec{r}}$ and $\tilde{C}_{\vec{r},-\vec{r}}$ become almost equal for intensities of several tens of photons per pixel and $\tilde{C}_{\vec{r},\vec{r}}$ becomes very slightly greater than $\tilde{C}_{\vec{r},-\vec{r}}$ for intensities greater than 300 photons per pixel. This evolution confirms that quantum effects are more visible when thermal-like fluctuations are not too intense. It is not clear if the complete disappearance of quantum effects for high gains is physical or due to numerical accuracy problems. On the experimental side however, it is quite clear that the sub-shot noise level on the differences cannot be attained when the shot-noise fluctuations are very small compared to the thermal fluctuations